




RESEARCH ARTICLE

Research on workspace visual-based continuous switching sliding mode control for cable-driven parallel robots

Sen Qian , Zeyao Zhao, Pengfei Qian, Zhengyu Wang  and Bin Zi 

School of Mechanical Engineering, Hefei University of Technology, Hefei, Anhui, China

Corresponding author: Zhengyu Wang; Email: wangzhengyu_hfut@hfut.edu.cn

Received: 20 April 2023; **Revised:** 10 August 2023; **Accepted:** 31 August 2023; **First published online:** 25 September 2023

Keywords: Cable-driven parallel robot; trajectory tracking; motion control; sliding mode control; Simulink-ADAMS co-simulation

Abstract

Achieving the high-precision control of cable-driven parallel robots (CDPRs) is complex because of their structural properties. In this paper, a quintessential redundant CDPR is designed as the research subject, and a continuous switching sliding mode controller based on workspace vision is implemented to enhance the accuracy and stability of trajectory tracking. In addition, a virtual prototype of the CDPR with uncertainties is created in the simulation analysis software ADAMS, and co-simulation is performed with the control system designed in Simulink to validate the effectiveness of the proposed control strategy. Furthermore, a CDPR platform is established for trajectory tracking experiments using the visual-based position feedback method. The trajectory tracking performance with the three control schemes is then evaluated. The experimental results show that the continuous switching sliding mode control algorithm can significantly decrease trajectory tracking errors and exhibit superior trajectory tracking performance compared to the other control strategies.

1. Introduction

As a specially constructed parallel robot, cable-driven parallel robots (CDPRs) utilize cables instead of rigid structures to connect moving platforms and drive equipment and integrate cable-driven kinematic chains and parallel mechanism theory [1]. CDPRs inherit the high-speed and high-load capabilities of parallel robots and have the advantages of low cost, simple structure, large working space, easy disassembly and reconfiguration, and low moment of inertia [1–3]. For several decades, CDPRs have been commonly utilized in many fields, such as tomography scanning and visual surveillance [4], additive manufacturing of building materials [5, 6], 500-calibre spherical radio telescope [7], wind tunnel tests [8], remotely manipulated tasks [9], human–robot co-manipulation [10], and rehabilitation training [11]. In this paper, a CDPR prototype for 3D printing tasks is designed and constructed. Leveraging various advantages of CDPR, this type of CDPR can be reconfigured in a wide range of scenarios to accomplish additive manufacturing of building materials in large-scale spaces in the future [12]. Although CDPRs have received more attention in recent years due to their various advantages, research on CDPRs still needs to be conducted to overcome various problems associated with their structural properties.

At present, a major challenge in CDPR research is tension distribution. Due to the unidirectional force properties, the cable tension must be positive. However, the calculation results show that the cable tension of CDPRs may have negative values or even no solution. In response to this situation, the number of cables is appropriately increased to make the mechanism redundant. The cable tension of a redundant CDPR has infinite solutions, so the tension distribution algorithm can be used to optimize the cable tension. Generally, the methods for calculating the optimal tension distribution include 1-norm, 2-norm, p-norm, centroid, and quantitative optimizations [1]. However, due to the complexity of most tension distribution algorithms, most algorithms entail substantial computational costs, which results in the

compromised real-time performance of feedback control. Currently, several algorithms, such as [12] and [13], can reduce the computational complexity of cable tension distributions to guarantee real-time performance. Moreover, some methods have been proposed to guarantee real-time performance. Ref. [14] adopted the offline tension distribution and proposed the tension control loop, reducing the dependence on real-time feasibility.

Another major research topic of CDPR is high-precision motion control. Due to the deformation of the cables and nonlinear friction, it is difficult to accurately represent CDPR dynamics with mathematical modelling. Additionally, the low stiffness of the cables results in low-frequency natural vibrations of the moving platform [15], which constrains the trajectory tracking accuracy of CDPRs and makes their motion control more complicated. To address these limitations, it is essential to identify the source of uncertainty in CDPRs. For example, [16] explored the influence of fixed pulley radii on the cable length error and proposed an uncertainty analysis method based on evidence theory. Moreover, closed-loop control methods can converge the errors caused by uncertainty. Various control methods are used in CDPRs, including PID [17, 18], robust control [19], reinforcement learning [20], neural networks [21], and adaptive control [22]. Sliding mode control (SMC) is an effective method for controlling nonlinear and uncertain systems and has considerable robustness to external disturbances and uncertain dynamics modelling [23]. For example, the SMC strategy can be utilized to compensate for the uncertainty caused by cable flexibility [24]. Additionally, there are many improved SMC strategies for CDPRs. Implementing a fuzzy adaptive algorithm for the SMC strategy can further reduce the impacts of uncertainties [25]. The second-order SMC strategy can strike a balance between improving the accuracy and reducing high-frequency chattering [26]. Designing the sliding surface as a nonlinear function enables the terminal SMC algorithm to achieve a faster convergence speed [27]. The CDPR proposed in this paper designed for additive manufacturing needs to address challenges related to motion platform vibrations caused by cable flexibility and reduced printing accuracy due to modelling uncertainties. SMC inherently possesses robustness against changes in system parameters, modelling error, and unmodelled disturbances compared to many other control methods, which enables it to effectively enhance the stability and motion precision of the moving platform.

There are two types of position feedback control for CDPRs: feedback control of the cable length space and feedback control of the task space. In [28], the cable length is regarded as the feedback value, which is an indirect feedback control based on the cable length space. In fact, controlling CDPRs with high accuracy is to improve the motion performance of the moving platform in the workspace [29] but not the cable length. Therefore, the control accuracy obtained in cable length space is not as reliable as that in the workspace. In [30], the pose of the mobile platform is directly measured by a multi-camera perception system as the feedback value of the control strategy. However, the camera calibration in this paper is complicated, and additional algorithms are required to convert the data from multiple cameras into pose information. Therefore, to achieve high-precision trajectory tracking performance, an easy-to-operate visual feedback method of the task space is needed. In summary, the principal contributions of this paper are as follows:

- An improved sliding mode control strategy is presented to mitigate the influence of the uncertainty of the CDPR system on the trajectory tracking performance. Instead of the noncontinuous switching function used in traditional SMC algorithms, the continuous switching SMC adopted in this paper effectively reduces the chattering phenomenon.
- An effective simulation verification method is established, in which Simulink can be used to intuitively and flexibly build the control model, while the mechanical system simulation software ADAMS can accurately simulate the complexity and uncertainty of the CDPR and achieve simulation visualization.
- Experiments are conducted to verify the trajectory tracking capacity of the designed control algorithm for the CDPR, and a position feedback method based on the workspace of the moving platform is designed. Six Nokov Mars series motion capture cameras are used in this method to capture the pose information of the moving platform in real time, and the collected pose data are fed back to the controller.

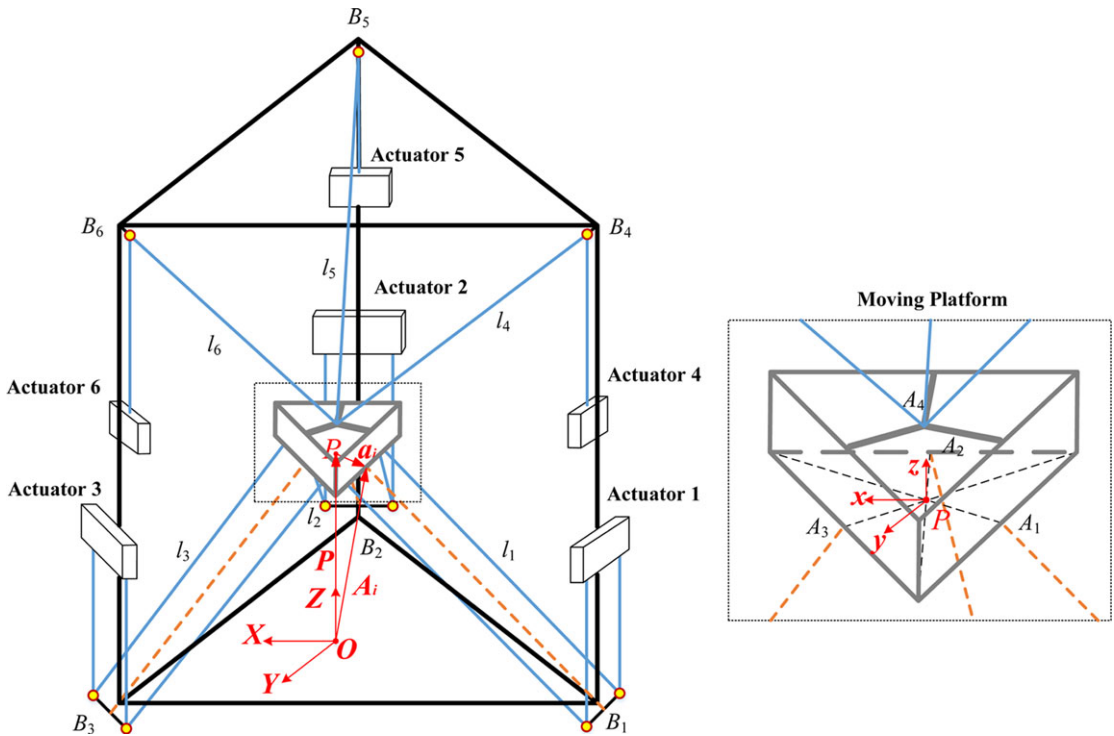


Figure 1. Structure of the CDPR platform.

The remainder of this paper is arranged as follows. Mathematical models of the kinematics and dynamics of CDPRs are established, and the solution formula of the cable tension is derived in Section 2. Then, in Section 3, continuous switching sliding mode control based on the hyperbolic tangent function (SMC-HT) is proposed, and the system stability is proven through the Lyapunov function. In Section 4, the validity and soundness of the SMC-HT strategy are demonstrated, and the cable tension is ensured to be positive. Moreover, a virtual prototype of a CDPR is established in ADAMS, and the SMC-HT strategy is developed in Simulink. In Section 5, a trajectory tracking experiment is implemented on the CDPR platform using the SMC-HT strategy. Finally, in Section 6, the paper is summarized, and a conclusion is provided.

2. Analysis of the mathematical models

2.1. Analysis of the kinematics

The CDPR structure model is shown in Fig. 1, in which the ends of the upper three cables are linked to a point on the moving platform and the other ends are connected to the pulleys fixed on the upper part of the CDPR frame. The lower six cables are organized in groups of two cables, with each cable in a group running parallel to the other. One end of each cable is connected to the moving platform, and the other end is attached to a pulley below the CDPR frame. There are six actuators within the CDPR structure, of which actuators 1, 2, and 3 are connected to the lower three groups of cable and actuators 4, 5, and 6 are connected to the upper three cables. All the actuators are connected to lead screws and powered by motors. In the subsequent calculation, we consider each pair of parallel cables below as an equivalent cable located at the axis of symmetry between the parallel cables.

The global coordinate system $O-XYZ$ connecting the base and the local coordinate system $P-xyz$ fixed on the moving platform are established, and the position of the local coordinate system origin point in the global coordinate system is P . If i represents the i -th cable, the global coordinates of the

connection points between cables and moving platform are A_i , and the local coordinates are a_i . The global coordinates of the connection points between the cables and pulleys are B_i . The relationship between Global Coordinates A_i and Local Coordinates a_i can be expressed as

$$A_i = R a_i + P \tag{1}$$

where R is the rotation matrix from the local coordinate system to the global coordinate system, which can be described as

$$R = rot(z, \gamma) rot(y, \beta) rot(x, \alpha) = \begin{bmatrix} c\beta c\gamma & c\gamma s\alpha s\beta - c\alpha s\gamma & s\alpha s\gamma + c\alpha c\lambda s\beta \\ c\beta s\gamma & c\alpha s\gamma + s\alpha s\beta s\gamma & c\alpha s\beta s\gamma - c\gamma s\alpha \\ -s\beta & c\beta s\alpha & c\alpha c\beta \end{bmatrix} \tag{2}$$

In Matrix R , c and s represent cos and sin, respectively. l_i is denoted as the cable length vector, which can be written as

$$l_i = B_i - A_i = B_i - R_i a_i - P \tag{3}$$

Moreover, the cable length can be obtained as

$$l_i = \|B_i - R_i a_i - P\| \tag{4}$$

The unit direction vectors of the cables can be computed from

$$u_i = l_i / l_i \tag{5}$$

Generally, the angular velocity of a rigid body cannot be directly obtained by derivation of the angular rotation. According to the relationship between the angular velocity of the rigid body and the derivative of the attitude coordinates, the angular velocity of the rigid body is

$$\omega = E \dot{\theta} \tag{6}$$

where the angular velocity and the first derivative of the angular rotation θ with respect to time of the moving platform are denoted as ω and $\dot{\theta}$, respectively. E is the transformation matrix between the angular velocity vectors and angular rotation of the moving platform:

$$E = \begin{bmatrix} c\beta c\gamma & -s\gamma & 0 \\ c\beta s\gamma & c\gamma & 0 \\ -s\beta & 0 & 1 \end{bmatrix} \tag{7}$$

The velocity vector of the moving platform can be written as

$$\begin{bmatrix} v \\ \omega \end{bmatrix} = \begin{bmatrix} I & \\ & E \end{bmatrix} \begin{bmatrix} \dot{r} \\ \dot{\theta} \end{bmatrix} = E_1 \dot{q} \tag{8}$$

where, $r = [x \ y \ z]^T$ and $\theta = [\alpha \ \beta \ \gamma]^T$ are the position and posture vectors of the moving platform, respectively. Moreover, $v = [\dot{x} \ \dot{y} \ \dot{z}]^T$ is the linear velocity vector and ω is the angular velocity vector.

There are 6 cables on the CDPR, $\dot{l} = [\dot{l}_1 \ \dot{l}_2 \ \dots \ \dot{l}_6]^T$ is the time derivative of the cable length, which can be written as

$$\dot{l} = J^T E_1 \dot{q} \tag{9}$$

where J^T is the 6×6 -order kinematic Jacobian matrix of CDPR:

$$J^T = \begin{bmatrix} u_1 & u_2 & \dots & u_6 \\ (Ra_1) \times u_1 & (Ra_2) \times u_2 & \dots & (Ra_6) \times u_6 \end{bmatrix}^T$$

2.2. Analysis of dynamics

The force and torque equilibrium of the moving platform can be written as

$$\begin{cases} \sum_1^n \mathbf{f}_i + \mathbf{f}_p = 0 \\ \sum_1^n (\mathbf{R}\mathbf{a}_i \times \mathbf{f}_i + \boldsymbol{\tau}_i = 0 \end{cases} \tag{10}$$

where \mathbf{f}_p and $\boldsymbol{\tau}_i$ are the external force and torque of the moving platform, respectively. Moreover, $\mathbf{f}_i = f_i \mathbf{u}_i$ is the i -th cable tension vector, and f_i is the i -th cable tension. Eq. (10) expresses the static equilibrium of the CDPR and can be rewritten in matrix form as follows:

$$\mathbf{J} \cdot \mathbf{f} + \mathbf{w} = 0 \tag{11}$$

where $\mathbf{f} = [f_1 \ \dots \ f_6]^T$, $\mathbf{w} = [\mathbf{f}_p^T \ \boldsymbol{\tau}_p^T]^T$ and \mathbf{J} is the dynamic Jacobian matrix, which is denoted as $\mathbf{J} = \begin{bmatrix} \mathbf{u}_1 & \mathbf{u}_2 & \dots & \mathbf{u}_6 \\ \mathbf{R}\mathbf{a}_1 \times \mathbf{u}_1 & \mathbf{R}\mathbf{a}_2 \times \mathbf{u}_2 & \dots & \mathbf{R}\mathbf{a}_6 \times \mathbf{u}_6 \end{bmatrix}$.

The model of the CDPR dynamics can be given in the following form:

$$\mathbf{M}(\mathbf{q}) \ddot{\mathbf{q}} + \mathbf{C}(\mathbf{q}, \dot{\mathbf{q}}) \dot{\mathbf{q}} + \mathbf{G} + \mathbf{w}_d = -\mathbf{J} \cdot \mathbf{f} \tag{12}$$

where $\mathbf{q} = [\mathbf{r}^T \ \boldsymbol{\theta}^T]^T$, $\dot{\mathbf{q}} = [\mathbf{v}^T \ \boldsymbol{\omega}^T]^T$ and $\ddot{\mathbf{q}}$ are the derivatives of $\dot{\mathbf{q}}$. Moreover, $\mathbf{M}(\mathbf{q})$ is the inertial matrix, $\mathbf{C}(\mathbf{q}, \dot{\mathbf{q}})$ is the Coriolis and centripetal matrix, \mathbf{G} is the gravitational vector, and \mathbf{w}_d represents the unknown external disturbances.

2.3. Cable tension distribution

Based on the relationship between the number of cables and degrees of freedom, CDPRs can be classified into under-constrained, fully constrained, and redundantly constrained structures. When the relationship between the number of cables i and degree of freedom n satisfies $i > n + 1$, the CDPR structure is redundant, and its cable tension has an infinite number of solutions. Therefore, it is necessary to calculate the cable tension of the CDPR to ensure that the tension is within a suitable range. In this paper, the CDPR has a 3-DOF, and there are 6 cables after equivalence. Thus, the system is redundant. Regarding this system, the solution formula for the cable tension distribution can be determined by the static equation:

$$\mathbf{J} \cdot \mathbf{f} + \mathbf{w} = 0 \tag{13}$$

where Jacobian matrix can be rewritten as $\mathbf{J} = [\mathbf{u}_1 \ \mathbf{u}_2 \ \dots \ \mathbf{u}_6]$ for the CDPR that does not consider rotational DOFs. Eq. (13) has three equations and six unknowns, and the general solution is

$$\mathbf{f} = -\mathbf{J}^+ \mathbf{w} + (\mathbf{I} - \mathbf{J}^+ \mathbf{J}) \mathbf{F}_{ref} \tag{14}$$

where $\mathbf{I} \in R^{6 \times 6}$ is the 3-dimensional unit matrix, \mathbf{J}^+ is the Moore-Penrose pseudoinverse of matrix \mathbf{J} , $\mathbf{J}^+ \mathbf{w}$ is the minimum norm solution, and $(\mathbf{I} - \mathbf{J}^+ \mathbf{J}) \mathbf{F}_{ref}$ is the zero-space solution set of the equation. $\mathbf{F}_{ref} \in R^6$ is an arbitrary vector. Generally, the cable tension should be maintained within a positive range:

$$\mathbf{0} < \mathbf{f}_{min} < \mathbf{f} < \mathbf{f}_{max} \tag{15}$$

A positive range ensures that the tension is not too small to cause the cables to loosen or exceed the maximum allowable tension of the cables. In this paper, we consider the arbitrary vector \mathbf{F}_{ref} in Eq. (14) as the reference cable tension, and we adjust the reference value to ensure that the cable tension remains within the proper range.

3. Design of the controller

Proposed by Vadim I. Utkin in 1977 [31], sliding mode control (SMC) has a favourable control effect on the uncertain system and has strong robustness to uncertain parameters and external disturbances in the system. The precise mathematical model of CDPRs is challenging to establish due to errors in manufacturing and installing parts, cable deformation during operation, inaccuracies in establishing dynamic modelling, nonlinear friction between mechanisms, and other influencing factors. To reduce the impact of uncertainty of the CDPRs, the sliding mode control strategy can be used to guarantee convergence and improve the trajectory tracking accuracy.

3.1. Design of controller

The dynamic modelling of the 3-DOF CDPR can be written as

$$\mathbf{M}\ddot{\mathbf{x}} + \mathbf{G} + \mathbf{w}_d = \mathbf{w} \quad (16)$$

The position error of the moving platform of the CDPR is

$$\mathbf{e}(t) = \mathbf{x}_d(t) - \mathbf{x}(t) \quad (17)$$

The sliding surface can be defined as

$$\mathbf{s}(t) = \dot{\mathbf{e}}(t) + \Lambda \mathbf{e}(t) \quad (18)$$

where $\dot{\mathbf{e}}$ is the derivative of the position error \mathbf{e} and $\Lambda = \text{diag}\{\Lambda_1 \ \Lambda_2 \ \Lambda_3\}$ is a positive-definite matrix. We choose the exponential approach sliding mode control; thus, the sliding mode surface approach law is designed as

$$\dot{\mathbf{s}}(t) = -\mathbf{K} \cdot \mathbf{s} - \eta \cdot \tanh\left[\frac{\mathbf{s}(t)}{\varepsilon}\right] \quad (19)$$

Furthermore, the reference velocity is defined as

$$\dot{\mathbf{x}}_r(t) = \dot{\mathbf{x}}_d(t) + \Lambda \mathbf{e}(t) \quad (20)$$

The reference acceleration can be obtained by differentiating Eq. (20):

$$\ddot{\mathbf{x}}_r(t) = \ddot{\mathbf{x}}_d(t) + \Lambda \dot{\mathbf{e}}(t) \quad (21)$$

The sliding mode control law can be expressed as

$$\mathbf{F}_x = \mathbf{M} \cdot \ddot{\mathbf{x}}_r(t) + \mathbf{G} + \mathbf{K} \cdot \mathbf{s}(t) + \eta \cdot \tanh\left[\frac{\mathbf{s}(t)}{\varepsilon}\right] \quad (22)$$

Substituting (22) into (14), the cable tension can be obtained as:

$$\mathbf{f} = \mathbf{J}^+ \left[\mathbf{M} \cdot \ddot{\mathbf{x}}_r(t) + \mathbf{G} + \mathbf{K} \cdot \mathbf{s}(t) + \eta \cdot \tanh\left(\frac{\mathbf{s}(t)}{\varepsilon}\right) \right] + (\mathbf{I} - \mathbf{J}^+ \mathbf{J}) \mathbf{F}_{ref} \quad (23)$$

where \mathbf{f} is the vector of 6 cable tensions, $\dot{\mathbf{x}}_d$ and $\ddot{\mathbf{x}}_d$ are the desired velocity and acceleration, respectively, $\mathbf{K} = \text{diag}\{k_1 \ k_2 \ k_3\}$ is a positive-definite matrix, $\varepsilon > 0$, and $\eta \geq \|\mathbf{w}_d\|$. Due to the discontinuous property of the signum function, it is difficult to eliminate the chattering of the sliding mode control. The proposed sliding mode controller uses the hyperbolic tangent function instead of the commonly used sign function, which can effectively reduce the oscillatory behaviour [32]. By adjusting the size of the parameter ε , the steepness of the hyperbolic tangent function can be adjusted. Finally, the controller frame is shown in Fig. 2.

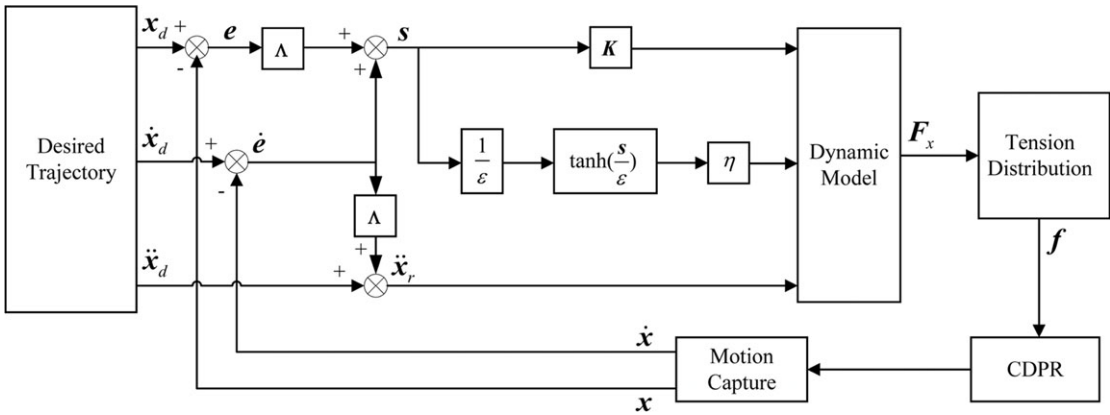


Figure 2. Control frame of SMC-HT strategy.

3.2. Analysis of the stability

Substituting (22) into (16) yields

$$M \cdot \ddot{x} + G + w_d = M \cdot \ddot{x}_r(t) + G + K \cdot s(t) + \eta \cdot \tanh\left[\frac{s(t)}{\epsilon}\right] \tag{24}$$

Differentiating the sliding surface (18) with respect to time yields:

$$\dot{s}(t) = \ddot{e}(t) + \Lambda \dot{e}(t) \tag{25}$$

Substituting Eq. (21) and Eq. (25) into Eq. (24) yields

$$M \cdot \dot{s}(t) + K \cdot s(t) + \eta \cdot \tanh\left[\frac{s(t)}{\epsilon}\right] - w_d = 0 \tag{26}$$

Since **M** is a positive-definite matrix, the Lyapunov function can be defined as

$$V = \frac{1}{2} s^T M s \tag{27}$$

Reference [33] provides the following inequation, which holds for any $\epsilon > 0$.

$$s^T \tanh\left(\frac{s}{\epsilon}\right) \geq \|s\| - \mu \epsilon \tag{28}$$

where μ is a constant that satisfies $\mu = e^{-(\mu+1)}$, that is, $\mu = 0.2785$. Differentiating *V* with respect to time in Eq. (27), then substituting Eq. (28) and known condition $\eta \geq \|w_d\|$ into it yields

$$\begin{aligned} \dot{V} &= s^T M \dot{s} = s^T \left[-K \cdot s - \eta \cdot \tanh\left(\frac{s}{\epsilon}\right) + w_d \right] \\ &= -s^T K s - \eta s^T \tanh\left(\frac{s}{\epsilon}\right) + s^T w_d \\ &\leq -s^T K s - \eta \|s\| + \mu \eta \epsilon + s^T w_d \\ &\leq -s^T K s + \mu \eta \epsilon \\ &\leq -\lambda_{\min}(K) s^T s + \mu \eta \epsilon \\ &= -2 \frac{\lambda_{\min}(K)}{\lambda(M)} \cdot \frac{1}{2} \lambda(M) s^T s + \mu \eta \epsilon \\ &= -2\lambda V + b \end{aligned} \tag{29}$$

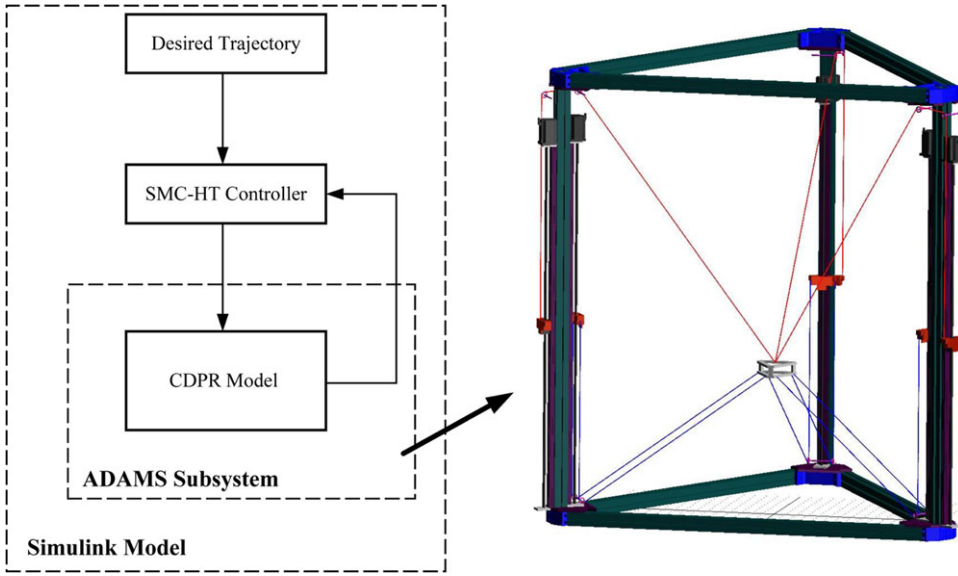


Figure 3. Simulation process.

where $\lambda_{\min}(\mathbf{K})$ is the minimal eigenvalue of \mathbf{K} , $\lambda(\mathbf{M})$ is the eigenvalue of \mathbf{M} , $\lambda = \frac{\lambda_{\min}(\mathbf{K})}{\lambda(\mathbf{M})}$, $b = \mu\eta\varepsilon$. Solving the differential inequality (29) yields

$$V(t) \leq e^{-2\lambda(t-t_0)} V(t_0) + \frac{b}{2\lambda} (1 - e^{-2\lambda(t-t_0)}) \tag{30}$$

Then, the following is obtained:

$$\lim_{t \rightarrow \infty} V(t) \leq \frac{\mu\eta\varepsilon}{2\lambda} \tag{31}$$

According to Eq. (31), the sliding mode function s is bounded; thus, the tracking error e and the differentiation of the tracking error \dot{e} are bounded. Moreover, \dot{e} is uniformly continuous, and $\dot{e} \rightarrow 0$ as $t \rightarrow \infty$, according to Barbara’s lemma. Therefore, e and \dot{e} are asymptotically convergent, and the convergence accuracy is related to ε , \mathbf{K} and η (i.e., w_d).

4. Simulation analysis

A simulation test was conducted on the CDPR virtual prototype using the Simulink-ADAMS co-simulation method to validate the effectiveness of the SMC-HT strategy for the CDPR virtual prototype and to observe changes in the cable tension. First, the CDPR model established in SolidWorks is imported into the mechanical system dynamics analysis software ADAMS. Then, the cable system, constraints, and driving force are set up in ADAMS to establish the virtual prototype of the CDPR. Next, the input and output variables are created to achieve data exchange with Simulink. Finally, the virtual prototype is exported to Simulink through the mechanical system export function provided in ADAMS, and the control system model is established in Simulink. The control system model and ADAMS virtual prototype are shown in Fig. 3. It is assumed that the cables in the virtual prototype have no deformation and no mass.

A certain space curve is adopted as the expected trajectory to evaluate the control performance of the CPDR, as shown in Fig. 4. Additionally, the component of the motion trajectory in the x-y plane

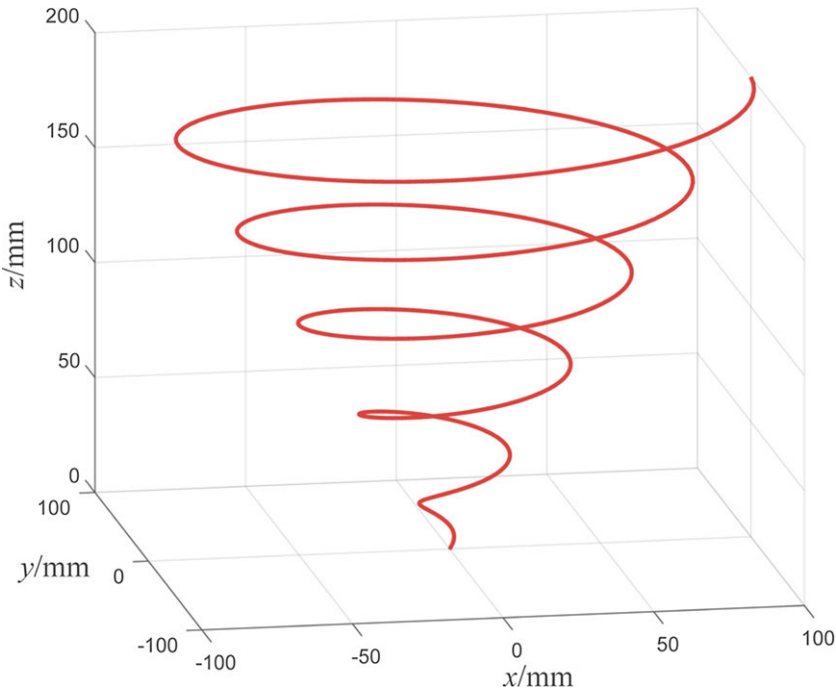


Figure 4. Desired trajectory of spiral.

is the Archimedes spiral, and the vertical direction is a uniform linear motion. The motion trajectory parameter equation can be expressed as Eq. (32).

$$\begin{cases} x = 10t \cos(\pi t) \\ y = 10t \sin(\pi t) \\ z = 20t \end{cases} \tag{32}$$

The simulation is set to a 0.025 s fixed step, and the parameters are manually set to make the trajectory tracking performance as optimal as possible. The parameters are tuned as follows: the hyperbolic tangent function steepness and gain parameters are $\eta = 0.3$ and $\varepsilon = 0.1$, respectively, the sliding surface parameter is $\Lambda = \text{diag}\{15 \ 15 \ 15\}$, the reference cable tension is $F_{ref} = [10 \ \dots \ 10]^T$, and the proportional gain matrix is $K = \text{diag}\{30 \ 30 \ 30\}$.

The PID control strategy based on gravity compensation and the open-loop control (OLC) strategy are compared with the proposed SMC-HT control strategy to verify the trajectory tracking performance of SMC-HT. The designed PID control law based on gravity compensation is as follows:

$$f = J^+ \left(K_p \cdot e + K_d \cdot \dot{e} + K_i \cdot \int e dx + G \right) + (I - J^+ J) F_{ref} \tag{33}$$

Similarly, the parameters of the PID control based on gravity compensation are set manually as $K_p = \text{diag}\{150 \ 150 \ 100\}$, $K_i = \text{diag}\{2 \ 2 \ 0.1\}$, $K_d = \text{diag}\{10 \ 10 \ 10\}$ and $F_{ref} = [10 \ \dots \ 10]^T$.

Figure 5 depicts the trajectory tracking error curves of the moving platform for three different control methods: OLC, PID, and SMC-HT. By comparing the curves of three different control strategies, it is evident that open-loop control has inferior trajectory tracking performance due to the modelling error and the friction between the mechanisms set in ADAMS. Additionally, the z-axis component experiences harmonic vibrations. Moreover, compared with OLC, although both PID and SMC-HT have good

Table I. *RSMEs of the spiral trajectory in the simulation.*

	<i>x</i> mm	<i>y</i> mm	<i>z</i> mm	α 10^{-3} deg	β 10^{-3} deg	γ 10^{-3} deg
OLC	1.467	1.023	7.567	4.689	8.211	8.172
PID	0.936	0.907	0.763	4.678	8.190	8.154
SMC-HT	0.211	0.208	0.331	4.573	8.006	7.971

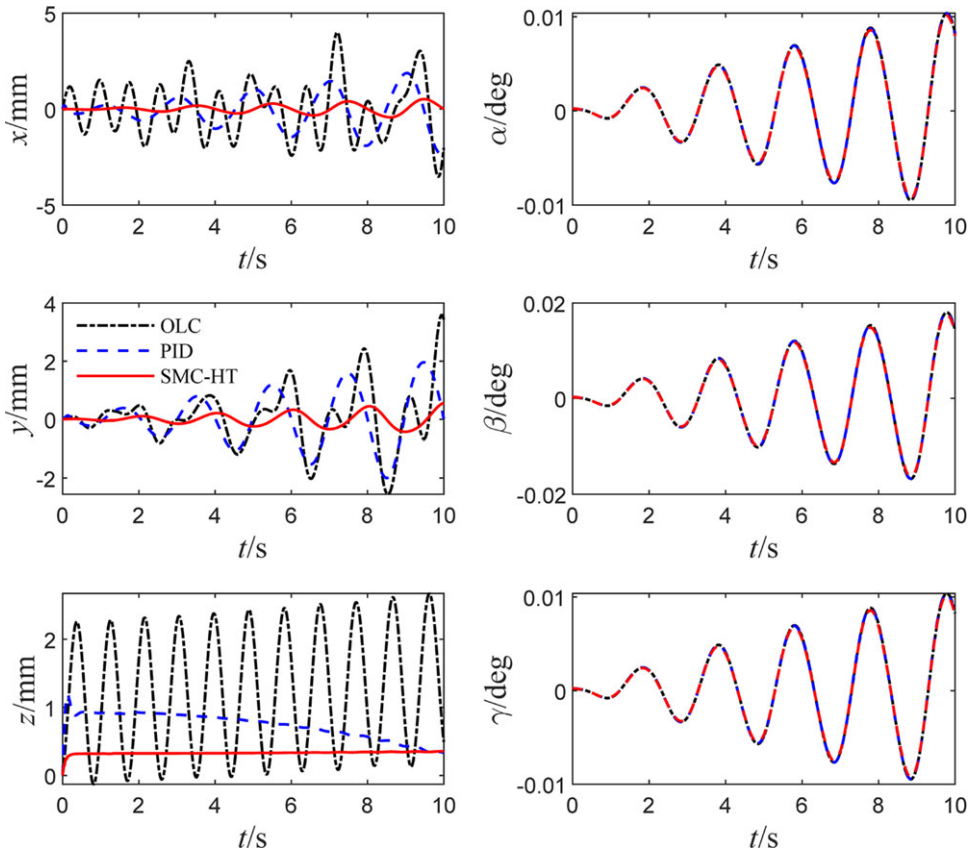


Figure 5. *Spiral trajectory tracking errors in the simulation.*

control effects, SMC-HT has a better trajectory tracking performance, smaller tracking error and more stable motion process. To further assess the effectiveness of the three different control strategies, the errors of the three control strategies are quantified, and the root mean square errors (RMSEs) of the trajectory tracking of the six axes are calculated, as shown in Table I. The statistical results confirm that the SMC-HT strategy has better trajectory tracking performance than the PID control strategy in translation, while the rotation error is not much different. This is because the rotational DOFs are not considered in our SMC-HT strategy. Furthermore, the simulation is subject to uncertainty due to errors that cannot be determined between ADAMS modelling and mathematical modelling. The results demonstrate that the SMC-HT strategy can effectively reduce the error to less than one millimetre, providing evidence of its effective control over uncertain systems.

The curves of the cable tension are shown in Fig. 6(a) and (b). Since F_{ref} in the tension distribution Eq. (14) can take any value, two different values of F_{ref} are selected for verification. Figure 6 indicates that by setting the reference value F_{ref} appropriately, the cable tension can always remain taut throughout

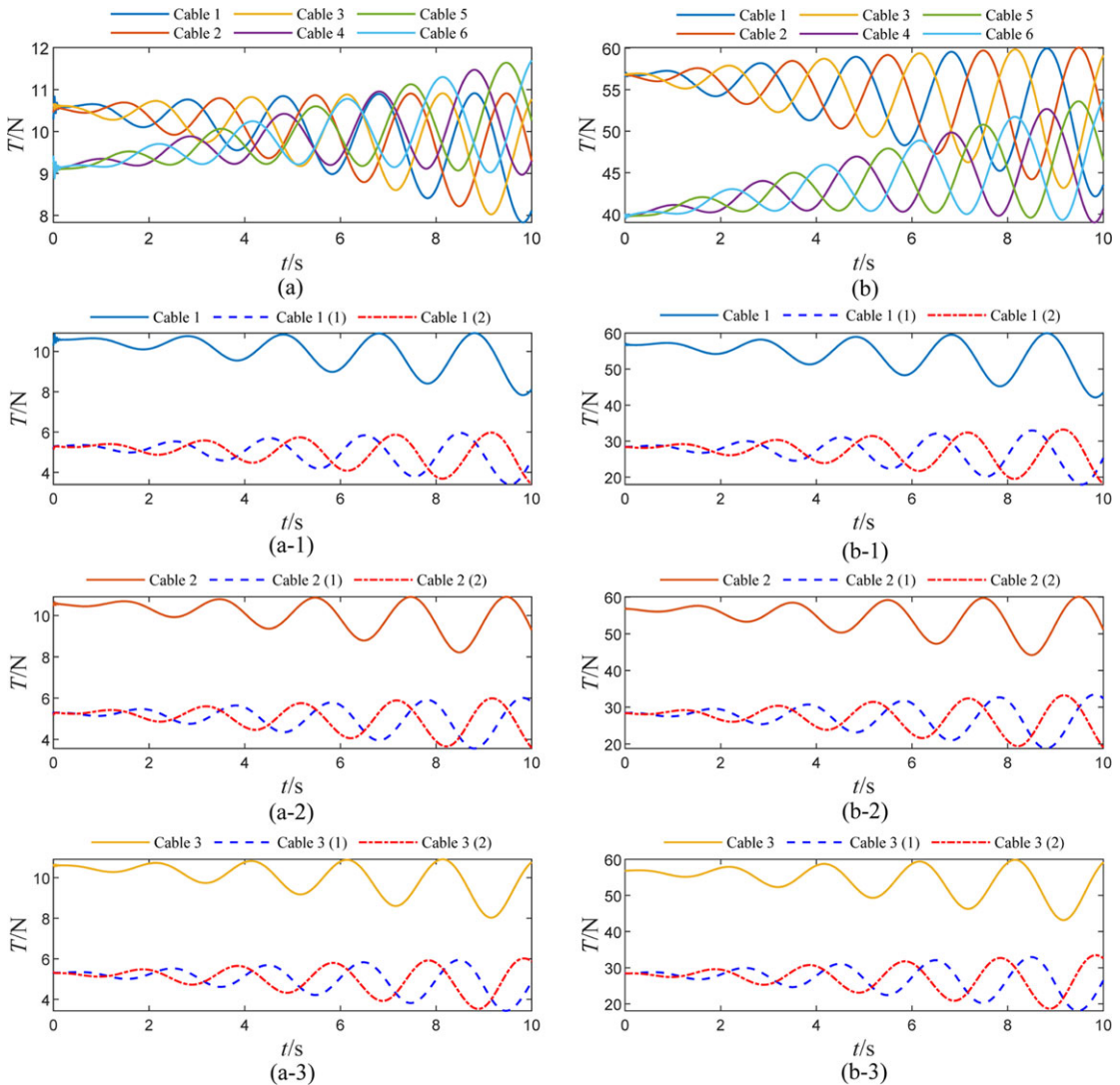


Figure 6. Cable tension of the CDPR. (a) $F_{ref} = 10\text{N}$, (b) $F_{ref} = 50\text{N}$.

the motion of the CDPR virtual prototype. In addition, the cable tension remained at approximately 10 N with a slight variation when $F_{ref} = 10\text{N}$. When $F_{ref} = 50\text{N}$, the cable tension is maintained at approximately 50 N, and the variation of the tension is more considerable. The trajectory errors of the moving platform when using the two different values of F_{ref} mentioned above are shown in Fig. 7, and both are obtained under the SMC-HT strategy. The results depicted in Fig. 7 indicate a significant rise in the trajectory errors of the moving platform and a tendency of the z-axis error curves to diverge when the cable tension is augmented. This is because the gain coefficient is unsuitable for the current system, and the parameters must be readjusted. In addition, the three rotation error curves show that the vibration amplitude of the moving platform increases significantly when the cable tension is higher. Since the control strategy does not include rotational DOFs, adjusting the gain coefficient cannot reduce the tilting degree of the moving platform. This indicates that a larger cable tension causes greater instability regardless of the gain parameters.

In Fig. 6 (a) and (b), the cables labelled as 1, 2, and 3 represent the equivalent cables, but each equivalent cable actually consists of two parallel cables. Figure 6 (a-1), (a-2), and (a-3) depict the actual

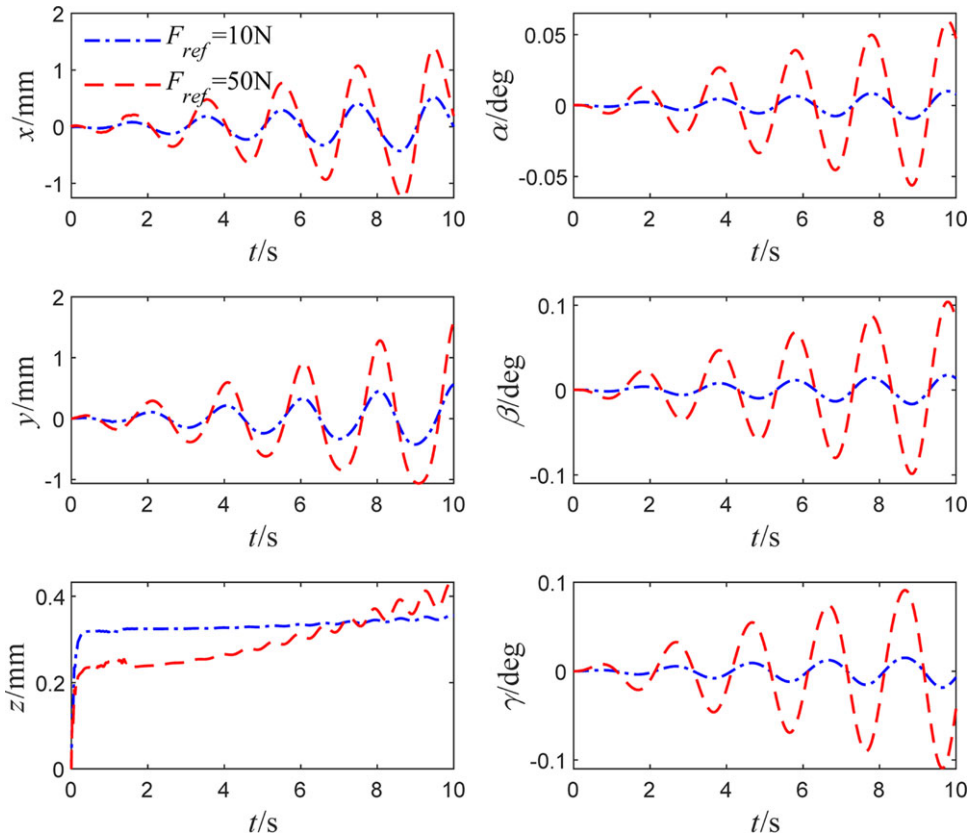


Figure 7. Tracking errors with different cable tensions.

tension curves of the two parallel cables 1, 2, and 3 when $F_{ref} = 10\text{N}$, respectively. Similarly, (b-1), (b-2), and (b-3) show the tension curves after decomposition for $F_{ref} = 50\text{N}$. In each diagram, the curve “Cable i ” ($i = 1, 2, 3$) represents the tension curve of the equivalent cable; “Cable i (1)” and “Cable i (2)” depict the actual tension curves of the two parallel cables in each group. From Fig. 6 (a-1) to (b-3), it can also be observed that the tensions of parallel cables in each group are not necessarily equal at all times. This is due to slight rotational displacement errors of the moving platform during operation (denoted as α , β , and γ in Fig. 7), causing varying extension lengths of the parallel cables. Based on the relationship between stress and strain, their tensions also differ. This further highlights the advantages of using the ADAMS software to establish a CDRP simulation model: specific parameters such as Young’s modulus of cable can be configured within the cable system in ADAMS, allowing for a more realistic simulation. After calculations, the tensions of the parallel cables also satisfy the following conditions:

$$T_i(t) = T_{i(1)}(t) + T_{i(2)}(t) \quad (i = 1, 2, 3) \tag{34}$$

where $T_i(t)$ represents the equivalent cable tension, while $T_{i(1)}(t)$ and $T_{i(2)}(t)$ represent the actual tensions of the two parallel cables in each group. This means the sum of the actual tensions of the parallel cables is equal to the tension of the equivalent cable at any given moment.

5. Experimental results

5.1. Device settings

The correctness of the proposed SMC-HT strategy is validated, and the theoretical trajectory tracking performance is tested in a previous simulation of the CDRP virtual prototype. In this section, further

Table II. Hardware and model of the experiment.

Hardware	Model
Industrial PC	Beckhoff C6650 (CPU Intel i7-6700)
Server Driver	Beckhoff AX5201
Servo Motor	Beckhoff AM8031
EtherCAT Coupler	Beckhoff EK1100
Analog Acquisition Module	Beckhoff EL3064
Force Sensor	ZHONGNUO ZNLBM-10KG
Motion Capture Camera	Nokov MARS2H

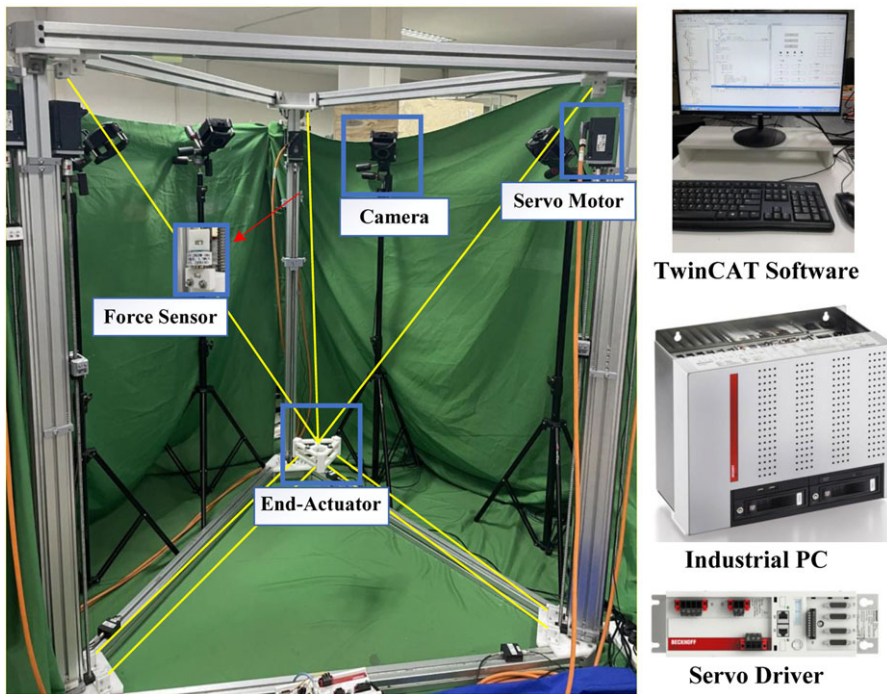


Figure 8. 6-cable 3-DOF CDPR platform.

experiments are performed on the experimental platform in which the SMC-HT algorithm is implemented. A CDPR of the 6-cable 3-DOF platform used in the experiments is shown in Fig. 8, and the moving platform has a weight of 1 kg. The three driving cables are linked to the upper part of the moving platform, which can drive the moving platform in the workspace, while the lower cables are the driven cables, which are used to maintain the stability of the moving platform. The maximum allowable tension of all cables is 150 N.

We use the Beckhoff hardware as the motion control solution, and the devices and models used are listed in Table II. Beckhoff TwinCAT 3 is used as the motion control software, and the EtherCAT coupler EK1100 and analogue acquisition module EL3064 collect the analogue signal of the force sensor. Then, the force signal can be received by TwinCAT. Moreover, the force data can be transmitted between Simulink and TwinCAT through the TE1410 module in TwinCAT. By writing the control law programme in MATLAB and transmitting calculated motor instructions to TwinCAT, MATLAB/Simulink can be used to directly control the platform. Then, the sensor signals are returned to Simulink, and the data can be processed in MATLAB/Simulink. The 6 motion capture cameras named Nokov are used to collect the pose data of the moving platform, which is easy to calibrate and has high accuracy (0.2 mm). The

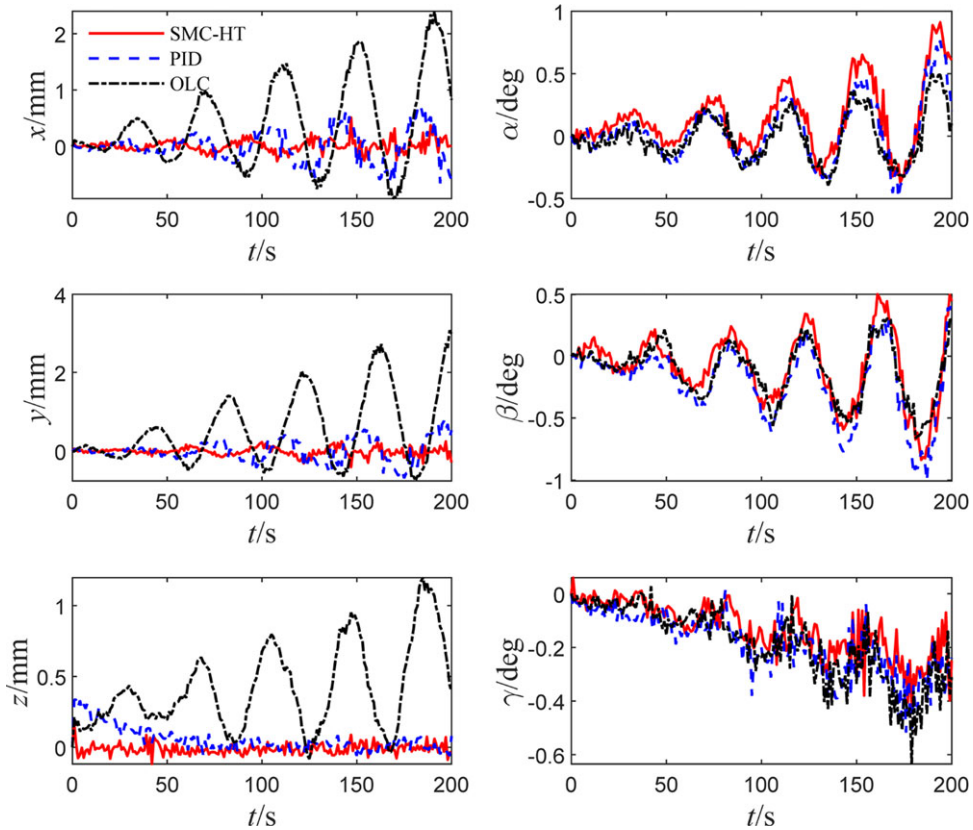


Figure 9. *Spiral trajectory tracking error in the experiment.*

real-time feedback function of posture is achieved by using the SDK of Cortex software to transmit data to Simulink. The software can receive and save the pose information of the moving platform captured by the motion capture system.

In the following two experiments, the CDPR’s trajectory tracking performance is evaluated using two different trajectories: a spiral trajectory and a space triangle trajectory composed of three point-to-point straight lines. The sampling periods for TwinCAT, Simulink, and Cortex are all set to 0.04 s. By manually adjusting the parameters, the gains of PID are set to $K_p = \text{diag}\{7.5 \ 7.5 \ 5\}$, $K_i = \text{diag}\{0.1 \ 0.1 \ 0.1\}$, $K_d = \text{diag}\{0.2 \ 0.2 \ 0.2\}$, and the parameters of SMC-HT are set to $K = \text{diag}\{4 \ 4 \ 4\}$, $\varepsilon = 0.02$, $\eta = 0.1$, $\Lambda = \{5 \ 5 \ 5\}$, $F_{ref} = [10 \ \cdots \ 10]^T$. The results of open-loop inverse dynamics, the PID control strategy based on gravity compensation and the SMC-HT strategy are compared to verify the trajectory tracking performance of the platform.

5.2. Spiral track experiment

In the spiral track experiment, the same curve as in the simulation is used as the desired motion track, which is expressed as the Eq. (35), and the motion time is set to 200 s.

$$\begin{cases} x = 0.5t \cos(0.05\pi t) \\ y = 0.5t \sin(0.05\pi t) \\ z = t \end{cases} \quad (35)$$

Figure 9 presents the pose error curves for three distinct control strategies. These curves closely resemble the error curves obtained through the simulation with respect to the displacement and rotation

Table III. *RSMEs of the spiral trajectory in the experiment.*

	<i>x</i> mm	<i>y</i> mm	<i>z</i> mm	α deg	β deg	γ deg
OLC	0.873	1.056	0.513	1.963	2.071	0.731
PID	0.281	0.287	0.099	3.108	3.216	1.012
SMC-HT	0.109	0.108	0.038	2.467	2.505	0.829

error curves of the moving platform. The implementation of a closed-loop control strategy in the system results in a significant reduction in the tracking errors of the moving platform. Compared to PID control, the proposed SMC-HT strategy has a smaller tracking error, higher precision and a more stable motion process, and its motion process is more stable. The *z*-axis error curve of the proposed SMC-HT strategy exhibits a faster convergence rate. Additionally, the tracking errors of the *x* and *y*-axes increase over time because the desired velocity of the spiral trajectory increases, while the tracking error for the *z*-axis reaches a steady state after a certain period. Moreover, since our three controllers do not involve the DOFs of rotation, there is little difference in the errors of the three rotational directions obtained by using the three control strategies. The trajectory tracking performances of the three control methods are further compared, and the RMSE statistics of the three control methods are shown in Table III, which further shows that the SMC-HT strategy has better trajectory tracking performance. Compared to OLC, the trajectory tracking error accuracy of the three axes *x*, *y*, and *z* increased by 87.5%, 89.72%, and 92.46%, respectively. Compared to the PID control strategy based on gravity compensation, the trajectory tracking error accuracy of the three axes increased by 61.29%, 62.24%, and 60.94%, respectively. Additionally, it can be observed that the SMC-HT strategy does not reduce the rotational RSMEs from Table III. This is because the control strategy proposed in this paper focuses on the control of translation of the moving platform, while the rotational DOFs remain in open-loop status. However, the results in Table III indicate that the SMC-HT control strategy proposed in this paper greatly improves the translation accuracy of the moving platform without significantly affecting the rotational performance.

During the operation of the CDPR, the lower three pairs of cables are redundant, which indicates that the stable operation of the moving platform is maintained, while the upper three cables are driving cables. Therefore, only the tension data of the upper three cables are collected in the experiment. The curves of the cable tension in the different control strategies are shown in Fig. 10, in which the trends of the cable tensions in the three driving cables are consistent with that of the simulated cable tension in the previous section (Cable 4, Cable 5 and Cable 6 in Fig. 6(a)), and the tension state of the cables is guaranteed.

5.3. Space triangle track experiment

In this experiment, a trajectory that is a space triangle composed of three straight lines is designed to evaluate the capacity of the three control strategies to maintain straight-line motion for the CDPR. As shown in Fig. 11, the trajectory passes through three points in sequence, and the coordinates of the three points are A(0, 0, 0), B(−140 mm, −80 mm, 300 mm), and C(100 mm, 150 mm, 100 mm). In each straight line, the desired velocity of the moving platform sinusoidally increases and reaches the maximum velocity of 10 mm/s. This velocity is maintained for a certain period and finally decreases to 0 sinusoidally.

The pose error curves of the space triangle trajectory of the three control strategies are illustrated in Fig. 12, and the RMSE statistics are presented in Table IV. The results are consistent with the experimental findings of the spiral track experiment, confirming that the proposed SMC-HT strategy achieves higher trajectory tracking accuracy. The accuracy of the *x*, *y* and *z* directions improves by 80.50%,

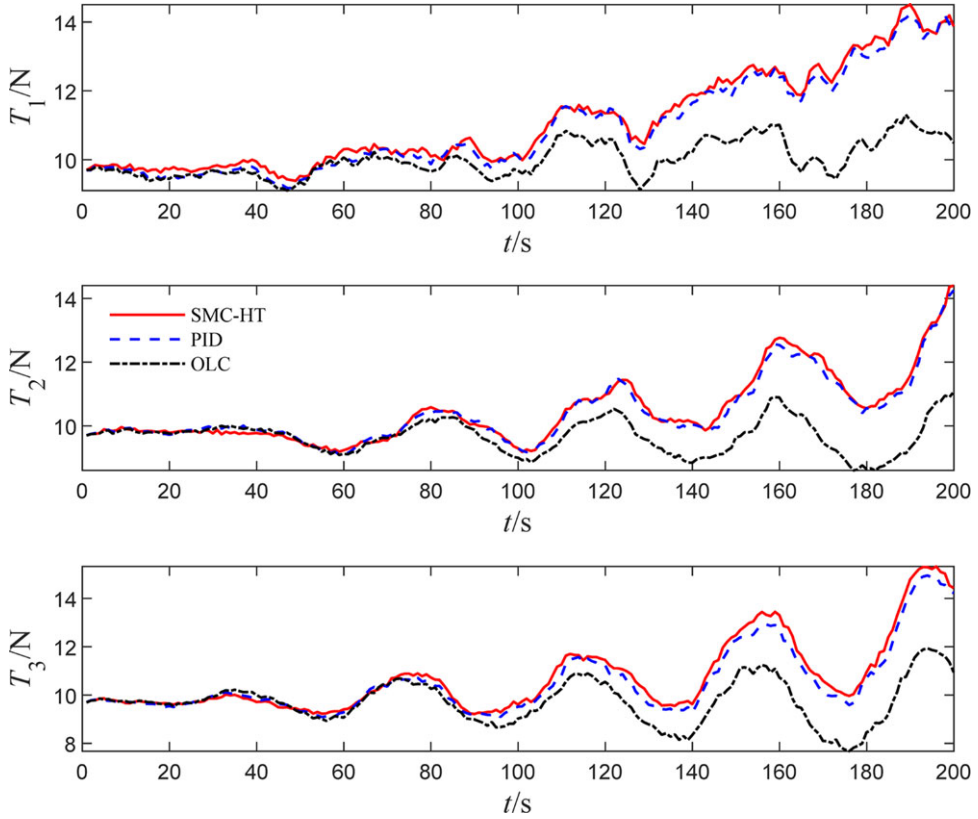


Figure 10. Cable tension with spiral trajectory in the experiment.

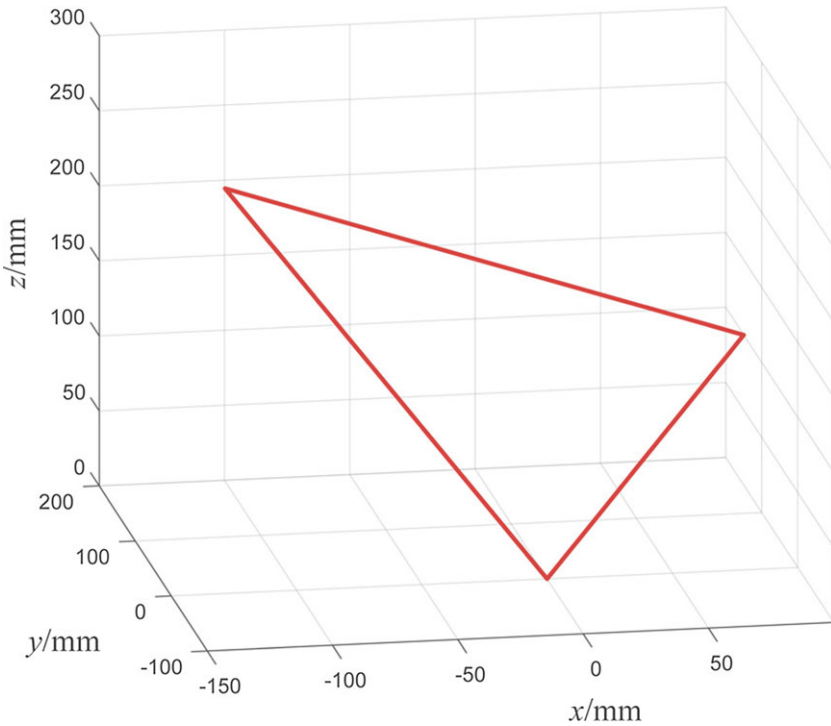


Figure 11. Desired trajectory of the space triangle.

Table IV. *RSMEs of the space triangle trajectory in the experiment.*

	x mm	y mm	z mm	α deg	β deg	γ deg
OLC	0.754	1.287	1.138	1.335	1.412	1.757
PID	0.337	0.342	0.424	1.275	1.341	1.939
SMC-HT	0.147	0.155	0.197	1.320	1.414	1.634

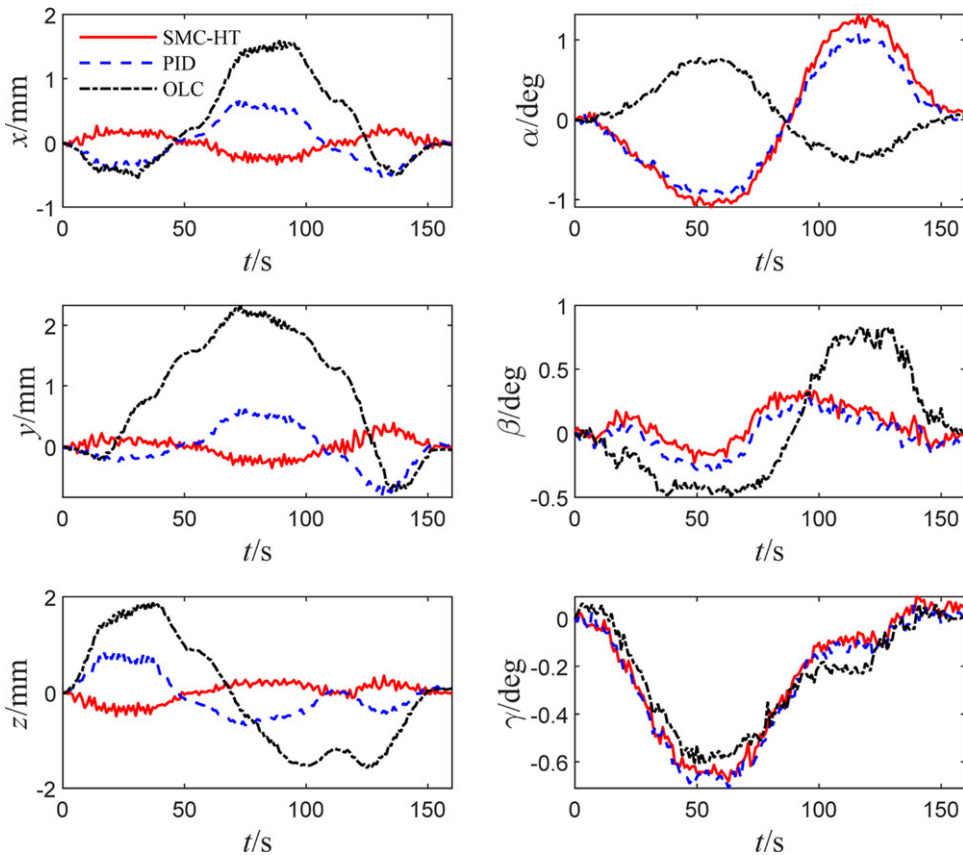


Figure 12. *Space triangle trajectory tracking errors in the experiment.*

87.96%, and 82.69%, respectively, compared to the OLC strategy and by 56.38%, 54.68%, and 53.54%, respectively, compared to the PID control strategy. Therefore, a higher velocity of the moving platform results in a higher error value. This rule also conformed to the error curves in the spiral trajectory experiment. Because the velocity of the spiral trajectory increases with time, the tracking errors of the moving platform also increase with time. While the velocity increases, the tracking error values increase less. Consequently, the regulation ability of the proposed SMC-HT strategy is better than that of the PID strategy. In addition, the cable tension curves are shown in Fig. 13. Moreover, when the PID and SMC-HT strategies are used, the forces of the three cables increase to varying degrees after the moving platform runs a complete cycle and returns to the origin. The SMC-HT method provides the most significant force increase. However, the maximum cable tension is below 14 N, which does not reach the maximum tension of 150 N allowed.

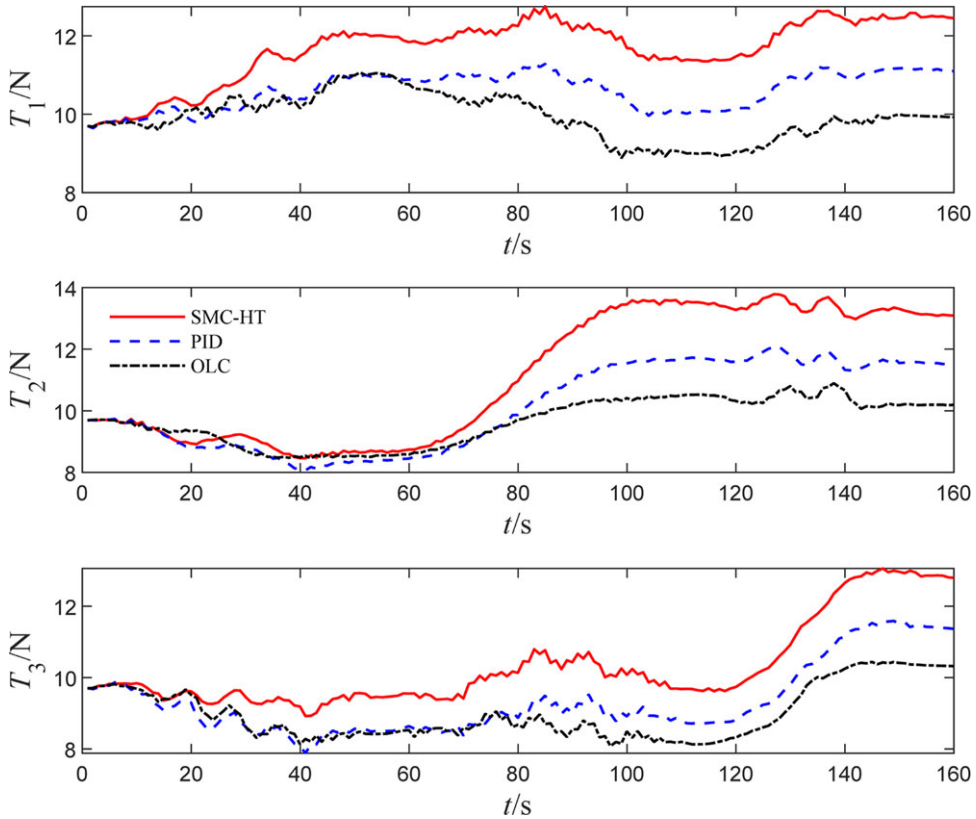


Figure 13. Cable tension of the space triangle trajectory in the experiment.

6. Conclusion

In this paper, mathematical models that are based on kinematics and dynamics are established to develop a novel 6-cable 3-DOF CDPD prototype, and the cable tension is calculated to ensure that the cables remain in a state of tension throughout the motion. In addition, we proposed an improved continuous switching sliding mode control algorithm (SMC-HT). The control algorithm utilizes the continuity of the hyperbolic tangent function to make the system slide smoothly along the sliding surface, which can effectively reduce system chattering. Afterwards, the stability of the control system of the SMC-HT strategy is proven through the Lyapunov function. In the ADAMS-Simulink co-simulation, compared to the PID control strategy based on gravity compensation, the SMC-HT strategy improves the accuracy of the x , y and z -axes by 77.46%, 77.07% and 61.61%, respectively. The two different trajectory experiments provided further evidence that the control strategy proposed has superior trajectory tracking performance compared to the PID control strategy based on gravity compensation. Regarding the SMC-HT control strategy, the accuracy of the three axes improved by 61.29%, 62.24%, and 60.94%, respectively, in the continuous spiral trajectory, while in the space triangle trajectory, the accuracy of the three axes improved by 56.38%, 54.68%, and 53.54%, respectively. The simulation and experimental results demonstrate the effectiveness of the SMC-HT strategy in reducing the impacts of model uncertainties on the trajectory tracking performance, improving the accuracy of the moving platform trajectory tracking, and increasing the system stability. Moreover, the SMC-HT strategy has a special compensation effect on the error caused by cable deformation because motion capture cameras are utilized to collect the position and posture data of the moving platform in the workspace and feedback to the controller directly. In the future, we will consider the rotational DOFs in the controller. Then, the SMC-HT algorithm will be considered for force and pose dual closed-loop control, and an adaptive algorithm will be designed to optimize the parameters of the controller.

Author contribution. Sen Qian, Zhengyu Wang, and Bin Zi conceived and designed the study. Zeyao Zhao and Pengfei Qian conducted data gathering. Zeyao Zhao performed statistical analyses. Sen Qian and Zeyao Zhao wrote the article.

Financial support. This work was supported by the National Key Research and Development Program of China (No. 2022YFB4702500) and the National Natural Science Foundation of China (Grant No.52175013, 51925502, U19A20101).

Competing interests. The authors declare no conflicts of interest exist.

Ethical approval. Not applicable.

References

- [1] Z. K. Zhang, Z. F. Shao, Z. You, X. Q. Tang, B. Zi, G. L. Yang, C. Gosselin and S. Caro, “State-of-the-art on theories and applications of cable-driven parallel robots,” *Front. Mech. Eng.* **17**(3), 37 (2022). doi: [10.1007/s11465-022-0693-3](https://doi.org/10.1007/s11465-022-0693-3).
- [2] S. Qian, B. Zi, W. W. Shang and Q. S. Xu, “A review on cable-driven parallel robots,” *Chin. J. Mech. Eng.* **31**(1), 66 (2018). doi: [10.1186/s10033-018-0267-9](https://doi.org/10.1186/s10033-018-0267-9).
- [3] M. Zarebidoki, J. S. Dhupia and W. L. Xu, “A review of cable-driven parallel robots typical configurations, analysis techniques, and control methods,” *IEEE Robot. Autom. Mag.* **29**(3), 89–106 (2022). doi: [10.1109/mra.2021.3138387](https://doi.org/10.1109/mra.2021.3138387).
- [4] S. Lessanibahri, P. Cardou and S. Caro, “A cable-driven parallel robot with an embedded tilt-roll wrist,” *ASME J. Mech. Rob.* **12**(2), 021107 (2020). doi: [10.1115/1.4045937](https://doi.org/10.1115/1.4045937).
- [5] P. C. Chesser, P. L. Wang, J. E. Vaughan, R. F. Lind and B. K. Post, “Kinematics of a cable-driven robotic platform for large-scale additive manufacturing,” *ASME J. Mech. Rob.* **14**(2), 021010 (2021). doi: [10.1115/1.4052010](https://doi.org/10.1115/1.4052010).
- [6] C. H. Lee and K. W. Gwak, “Design of a novel cable-driven parallel robot for 3D printing building construction,” *Int. J. Adv. Manuf. Technol.* **123**(11–12), 4353–4366 (2022). doi: [10.1007/s00170-022-10323-y](https://doi.org/10.1007/s00170-022-10323-y).
- [7] B. Y. Duan, “A new design project of the line feed structure for large spherical radio telescope and its nonlinear dynamic analysis,” *Mechatronics* **9**(1), 53–64 (1999). doi: [10.1016/s0957-4158\(98\)00028-2](https://doi.org/10.1016/s0957-4158(98)00028-2).
- [8] K. Y. Park, Y. H. Sung and J. H. Han, “Development of a cable suspension and balance system and its novel calibration methods for effective wind tunnel tests,” *Measurement* **170**, 108717 (2021). doi: [10.1016/j.measurement.2020.108717](https://doi.org/10.1016/j.measurement.2020.108717).
- [9] M. C. Kim, H. Choi, J. Piao, E. S. Kim, J. O. Park and C. S. Kim, “Remotely manipulated peg-in-hole task conducted by cable-driven parallel robots,” *IEEE-ASME Trans. Mechatron.* **27**(5), 3953–3963 (2022). doi: [10.1109/tmech.2022.3150108](https://doi.org/10.1109/tmech.2022.3150108).
- [10] M. Metillon, C. Charron, K. Subrin and S. Caro, “Performance and interaction quality variations of a collaborative Cable-Driven Parallel Robot,” *Mechatronics* **86**, 102839 (2022). doi: [10.1016/j.mechatronics.2022.102839](https://doi.org/10.1016/j.mechatronics.2022.102839).
- [11] Y. Mao, X. Jin, G. G. Dutta, J. P. Scholz and S. K. Agrawal, “Human movement training with a cable driven ARm EXoskeleton (CAREX),” *IEEE Trans. Neural Syst. Rehabil. Eng.* **23**(1), 84–92 (2015). doi: [10.1109/tnsr.2014.2329018](https://doi.org/10.1109/tnsr.2014.2329018).
- [12] H. B. Gao, G. Y. Sun, Z. Liu, C. Sun, N. Li, L. Ding, H. T. Yu and Z. Q. Deng, “Tension distribution algorithm based on graphics with high computational efficiency and robust optimization for two-redundant cable-driven parallel robots,” *Mech. Mach. Theory* **172**, 104739 (2022). doi: [10.1016/j.mechmachtheory.2022.104739](https://doi.org/10.1016/j.mechmachtheory.2022.104739).
- [13] X. Y. Geng, M. Li, Y. F. Liu, Y. Y. Li, W. Zheng and Z. B. Li, “Analytical tension-distribution computation for cable-driven parallel robots using hypersphere mapping algorithm,” *Mech. Mach. Theory* **145**, 103692 (2020). doi: [10.1016/j.mechmachtheory.2019.103692](https://doi.org/10.1016/j.mechmachtheory.2019.103692).
- [14] B. Zhang, W. W. Shang, S. Cong and Z. J. Li, “Dual-loop dynamic control of cable-driven parallel robots without online tension distribution,” *IEEE Trans. Syst. Man Cybern. Syst.* **52**(10), 6555–6568 (2022). doi: [10.1109/tsmc.2022.3146919](https://doi.org/10.1109/tsmc.2022.3146919).
- [15] L. Cuvillon, X. Weber and J. Gangloff, “Modal control for active vibration damping of cable-driven parallel robots,” *ASME J. Mech. Rob.* **12**(5), 051004 (2020). doi: [10.1115/1.4046434](https://doi.org/10.1115/1.4046434).
- [16] J. Gao, B. Zhou, B. Zi, S. Qian and P. Zhao, “Kinematic uncertainty analysis of a cable-driven parallel robot based on an error transfer model,” *ASME J. Mech. Rob.* **14**(5), 051008 (2022). doi: [10.1115/1.4053219](https://doi.org/10.1115/1.4053219).
- [17] H. An, Y. Zhang, H. Yuan, W. Xu and X. Wang, “Design control and performance of a cable-driving module with external encoder and force sensor for cable-driven parallel robots,” *ASME J. Mech. Rob.* **14**(1), 014502 (2021). doi: [10.1115/1.4051608](https://doi.org/10.1115/1.4051608).
- [18] C. Sancak, M. Itik and T. T. Nguyen, “Position control of a fully constrained planar cable-driven parallel robot with unknown or partially known dynamics,” *IEEE-ASME Trans. Mechatron.* **28**(3), 1605–1615 (2023). doi: [10.1109/tmech.2022.3228444](https://doi.org/10.1109/tmech.2022.3228444).
- [19] M. H. Barhaghtalab, H. Bayani, A. Nabaei, H. Zarrabi and A. Amiri, “On the design of the robust neuro-adaptive controller for cable-driven parallel robots,” *Automatika* **57**(3), 724–735 (2017). doi: [10.7305/automatika.2017.02.1793](https://doi.org/10.7305/automatika.2017.02.1793).
- [20] C. Sancak, F. Yamac and M. Itik, “Position control of a planar cable-driven parallel robot using reinforcement learning,” *Robotica* **40**(10), 3378–3395 (2022). doi: [10.1017/s0263574722000273](https://doi.org/10.1017/s0263574722000273).
- [21] H. Xiong, L. Zhang and X. M. Diao, “A learning-based control framework for cable-driven parallel robots with unknown Jacobians,” *Proc. Inst. Mech. Eng. Part I J. Syst. Control Eng.* **234**(9), 1024–1036 (2020). doi: [10.1177/0959651819898945](https://doi.org/10.1177/0959651819898945).
- [22] W. W. Shang, F. Xie, B. Zhang, S. Cong and Z. J. Li, “Adaptive cross-coupled control of cable-driven parallel robots with model uncertainties,” *IEEE Robot. Autom. Lett.* **5**(3), 4110–4117 (2020). doi: [10.1109/ra.2020.2988430](https://doi.org/10.1109/ra.2020.2988430).
- [23] H. G. Sage, M. F. de Mathelin and E. Ostertag, “Robust control of robot manipulators: A survey,” *Int. J. Control* **72**(16), 1498–1522 (1999). doi: [10.1080/002071799220137](https://doi.org/10.1080/002071799220137).

- [24] M. H. Korayem, M. Taherifar and H. Tourajizadeh, “Compensating the flexibility uncertainties of a cable suspended robot using SMC approach,” *Robotica* **33**(3), 578–598 (2015). doi: [10.1017/s0263574714000472](https://doi.org/10.1017/s0263574714000472).
- [25] B. Zi, H. H. Sun and D. Zhang, “Design, analysis and control of a winding hybrid-driven cable parallel manipulator,” *Robot. Comput. Integr. Manuf.* **48**, 196–208 (2017). doi: [10.1016/j.rcim.2017.04.002](https://doi.org/10.1016/j.rcim.2017.04.002).
- [26] H. Y. Jia, W. W. Shang, F. Xie, B. Zhang and S. Cong, “Second-order sliding-mode-based synchronization control of cable-driven parallel robots,” *IEEE-ASME Trans. Mechatron.* **25**(1), 383–394 (2020). doi: [10.1109/tmech.2019.2960048](https://doi.org/10.1109/tmech.2019.2960048).
- [27] A. Ameri, A. Molaei, M. A. Khosravi and M. Hassani, “Control-based tension distribution scheme for fully constrained cable-driven robots,” *IEEE Trans. Ind. Electron.* **69**(11), 11383–11393 (2022). doi: [10.1109/tie.2021.3125657](https://doi.org/10.1109/tie.2021.3125657).
- [28] W. Lv, L. Tao and Z. Ji, “Sliding mode control of cable-driven redundancy parallel robot with 6 DOF based on cable-length sensor feedback,” *Math. Probl. Eng.* **2017**, 1–21 (2017). doi: [10.1155/2017/1928673](https://doi.org/10.1155/2017/1928673).
- [29] B. Zhang, W. Shang, S. Cong and Z. Li, “Coordinated dynamic control in the task space for redundantly actuated cable-driven parallel robots,” *IEEE-ASME Trans. Mechatron* **26**(5), 2396–2407 (2020). doi: [10.1109/tmech.2020.3038852](https://doi.org/10.1109/tmech.2020.3038852).
- [30] T. Dallej, M. Gouttefarde, N. Andreff, P. E. Herve and P. Martinet, “Modeling and vision-based control of large-dimension cable-driven parallel robots using a multiple-camera setup,” *Mechatronics* **61**, 20–36 (2019). doi: [10.1016/j.mechatronics.2019.05.004](https://doi.org/10.1016/j.mechatronics.2019.05.004).
- [31] V. I. Utkin, “Variable structure systems with sliding modes,” *IEEE Trans. Autom. Control* **22**(2), 212–222 (1977). doi: [10.1109/tac.1977.1101446](https://doi.org/10.1109/tac.1977.1101446).
- [32] M. P. Aghababa and M. E. Akbari, “A chattering-free robust adaptive sliding mode controller for synchronization of two different chaotic systems with unknown uncertainties and external disturbances,” *Appl. Math. Comput.* **218**(9), 5757–5768 (2012). doi: [10.1016/j.amc.2011.11.080](https://doi.org/10.1016/j.amc.2011.11.080).
- [33] M. M. Polycarpou and P. A. Ioannou, “A robust adaptive nonlinear control design,” *Automatica* **32**(3), 423–427 (1996). doi: [10.1016/0005-1098\(95\)00147-6](https://doi.org/10.1016/0005-1098(95)00147-6).